

Sorbonne Université – Faculté des Sciences et Ingénierie

Master Quantum processes, Optics and Matter - QuOM

Toward Constraining μ (proton-to-electron mass ratio) Variation: Molecular Transition Analysis and Optical Signal Stabilization

— Master's thesis —

StudentDiyaa Aboul Hosen

Supervisor
Laurent HILICO

Table of Contents

Contents

1	Abstract	2
2	Introduction	2
3	Molecular Structure and Spectroscopy of Ammonia3.1 Vibrational Modes of Ammonia3.2 Inversion Transition in Ammonia3.3 Ro-Vibrational Quantum Numbers and Selection Rules	
4	Probing Variations in μ: Overview of Current Work	8
5	Indirect Determination of MW/MMW Transitions via MIR Spectroscopy 5.1 Original Approach	10 10
6	Results and Analysis 6.1 Candidate Transition Schemes for Probing μ-variation	
7	Optical Signal Stabilization 7.1 Importance	22
8	Future Work and General Remarks 8.1 Future Perspectives	26 26

1 Abstract

Constraining the possible variation of fundamental constants such as the proton-to-electron mass ratio μ offers a powerful avenue to test the Einstein Equivalence Principle and search for new physics beyond the Standard Model. In this work, conducted within the framework of the Ultiµos project, I focused on identifying and characterizing high-sensitivity molecular transitions in ammonia (14 NH₃) that are both observable in the interstellar medium and highly sensitive to variations in μ .

I developed a Python-based tool to analyze the HITRAN molecular database, allowing the automated identification of transition schemes, primarily involving microwave (MW) and millimeter-wave (MMW) lines, that exhibit high sensitivity coefficients and are part of sequences potentially usable in laboratory experiments. I cross-validated these schemes against the literature to identify transitions previously observed in astrophysical environments. Among these, I proposed a new scheme involving two transitions, including a highly μ sensitive MMW transition, which is theoretically promising and confirmed observationally. The transition scheme I identified is, to our knowledge, the first to combine high theoretical sensitivity with proven extraterrestrial observability and reproducibility, laying the foundation for future laboratory measurements. This work forms a critical preparatory step towards establishing the most stringent constraints on the variation of μ .

In parallel, I implemented a phase noise compensation system for the Refimeve optical signal transmitted from LTE (former SYRTE), achieving a beatnote linewidth below 1 Hz - demonstrating excellent phase stability. This compensation is crucial for future high-resolution spectroscopy experiments.

2 Introduction

Molecules provide an excellent testing ground for probing potential variations of fundamental constants in physics. In particular, electronic transitions are sensitive to the fine-structure constant α , while vibrational, rotational, and inversion transitions respond to changes in the dimensionless proton-to-electron mass ratio $\mu = m_p/m_e$. If either of these constants were to vary over time or space, such variations would manifest as measurable shifts in the transition frequencies of certain molecular species.

These shifts can be explored using two complementary approaches: high-precision laboratory measurements conducted over short time scales (years) and astronomical observations of spectral lines from distant cosmic sources. The possibility that fundamental constants might vary on cosmological scales was first suggested by Dirac [1]. To date, there remains no theoretical justification for the specific values these constants take, nor any certainty that they have remained unchanged over the history of the universe.

Interest in this field grew considerably following reports of a possible temporal variation in the fine-structure constant. Observations of atomic absorption lines in quasar spectra suggested that α may have been slightly smaller in the past [2]. Later studies analyzing molecular hydrogen spectra (H₂) indicated that the proton-to-electron mass ratio μ might have been greater by approximately 0.002% up to 12

billion years ago [3]. However, most subsequent studies have returned null results, casting doubt on these early claims (see [4] for a comprehensive review).

Despite these null results, the potential detection of any variation in fundamental constants would have profound implications for modern physics. Such a discovery would point to a violation of the Einstein Equivalence Principle and necessitate physics beyond the Standard Model, possibly shedding light on the nature of dark matter or dark energy.

Among the most promising molecular candidates for probing variations in μ is ammonia ($^{14}NH_3$). Its rich spectrum of rotational-vibrational transitions includes specific modes that exhibit high sensitivity to μ -variation [5, 6, 7]. This sensitivity is quantified by a dimensionless coefficient $T_{u,l}$, defined as:

$$T_{u,l} = \frac{\mu}{E_u - E_l} \left(\frac{dE_u}{d\mu} - \frac{dE_l}{d\mu} \right) \tag{1}$$

where E_u and E_l are the energies of the upper and lower molecular states, respectively.

The corresponding relative frequency shift due to a change in μ is given by:

$$\frac{\Delta\nu}{\nu_0} = T_{u,l} \frac{\Delta\mu}{\mu_0},\tag{2}$$

where $\Delta \nu = \nu_{\rm obs} - \nu_0$ is the difference between the observed and laboratory frequencies, and $\Delta \mu = \mu_{\rm obs} - \mu_0$ represents a deviation of μ from its current laboratory value.

By comparing the laboratory-measured transition frequencies of ammonia with those observed in interstellar molecular clouds, one can place stringent constraints on the time and spatial variations of μ .

3 Molecular Structure and Spectroscopy of Ammonia

3.1 Vibrational Modes of Ammonia

Ammonia (¹⁴NH₃) is a non-linear polyatomic molecule composed of one nitrogen and three hydrogen atoms. It exhibits a pyramidal structure with the nitrogen atom at the apex and the three hydrogen atoms forming a base in a trigonal planar arrangement.

The molecule has a total of 3N = 12 degrees of freedom, where N is the number of atoms. These are distributed as follows:

- 3 translational degrees of freedom (center of mass motion),
- 3 rotational degrees of freedom (due to its non-linear geometry),
- 6 vibrational degrees of freedom, obtained from 3N 6 = 6.

Despite having six vibrational degrees of freedom, ammonia exhibits only four distinct vibrational modes, two of which are doubly degenerate (degeneracy D=2). These modes are summarized in Table 1 and described below:

• ν₁: Symmetric Stretch ("Breathing Mode")

In this mode, all three N–H bonds simultaneously stretch and contract in phase. It is a totally symmetric vibration with degeneracy 1.

• ν₂: Symmetric Bend ("Umbrella Mode")

This involves a concerted in-phase bending of the N–H bonds, where the hydrogen atoms move upward and downward, and the nitrogen atom oscillates oppositely. It is non degenerate.

Importantly, this mode is associated with a quantum tunneling effect: the nitrogen atom tunnels through the potential barrier formed by the plane of the three hydrogen atoms. This results in an **inversion splitting** of the vibrational energy levels, a key feature that will be further discussed below due to its significance in high-precision spectroscopy and in probing variations of fundamental constants.

• ν_3 : Asymmetric Stretch

In this doubly degenerate mode (D=2), two N–H bonds stretch while the third contracts, and vice versa, leading to out-of-phase motion. Since this motion is asymmetric and out of phase, it is associated with a vibrational angular momentum.

• ν_4 : Asymmetric Bend

Also doubly degenerate (D=2), this mode involves out-of-phase bending, where two N–H bonds bend in one direction and the third in the opposite. Similarly, due to the asymmetric and out-of-phase nature of this motion, there is an associated vibrational angular momentum.

Energy cm⁻¹ D Mode Description 3336.7 ν_1 (symmetric stretch) All N-H bonds stretch in and out (IN PHASE) 1 ν_2 (symmetric bend) H-N-H angles bend in a symmetric way 1 950.4 2 ν_3 (asymmetric stretch) 2 N–H bond stretches while the other compress 3443.8 2 H–N–H bending in opposite directions 1626.8 ν_4 (asymmetric bend)

Table 1: Vibrational Modes of Ammonia (NH₃).

These vibrational modes define the key energy levels in the vibrational spectrum of ammonia and play a crucial role in determining its infrared and microwave spectroscopic signatures.

In the following section, we will delve deeper into the **inversion transition** associated with the umbrella mode (ν_2), and its relevance in precision measurements, particularly in the context of constraining possible variations of fundamental constants.

3.2 Inversion Transition in Ammonia

The inversion motion in ammonia corresponds to the nitrogen atom tunneling through the plane defined by the three hydrogen atoms, effectively inverting the molecular configuration; see Fig.1. This quantum tunneling leads to a **splitting of vibrational energy levels**, observable as distinct lines in the spectrum. The two lowest inversion states form a doublet, whose separation depends on the shape of the double-well potential.

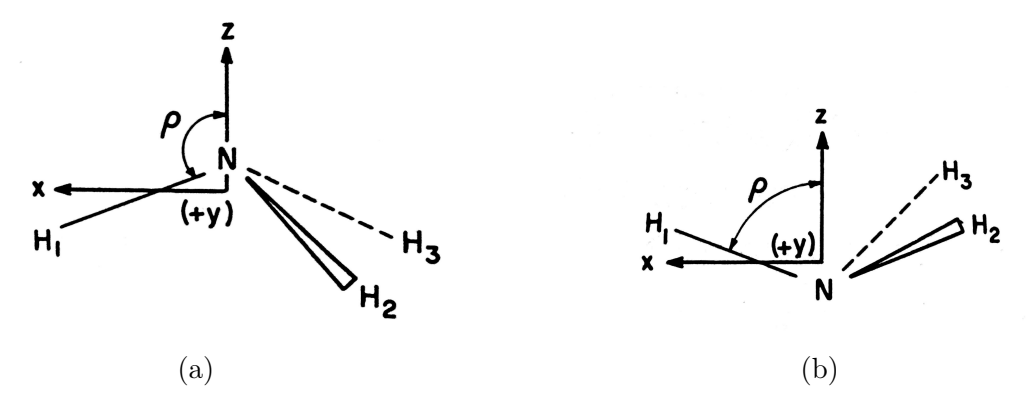


Figure 1: The reference configuration of NH_3 . The NH bond lengths are equal to their equilibrium values and the three HNH angles are equal to each other. The molecule fixed (x,y,z) axes are the principal inertial axes.

Fig. 2 shows the characteristic double-well potential and corresponding energy levels, as described in detail by Papoušek, Špirko, and Stone (1973), and Bunker (1975). Without tunneling, the situation would be as shown in Figure 3, where the states would remain degenerate.

The inversion splitting is especially small in the vibrational ground state, with a transition energy typically in the microwave (MW) domain, on the order of 0.1 to 10 cm^{-1} . This narrow spacing makes the inversion transition particularly valuable in high-precision spectroscopy. In astrophysics, for example, **radio telescopes operating in the MW and millimeter-wave (MMW) bands** can detect these lines with very high resolution, enabling detailed investigations of molecular clouds both in the Milky Way and in distant galaxies.

3.3 Ro-Vibrational Quantum Numbers and Selection Rules

To describe the energy levels of the ammonia molecule (NH₃), a comprehensive set of quantum numbers is employed, particularly as adopted in the HITRAN database [9]. These quantum numbers characterize the vibrational, rotational, and inversional degrees of freedom of the molecule, which is non-rigid and exhibits tunneling motion. In total, 13 quantum numbers are used:

$$\nu_1, \nu_2, \nu_3, l_3, \nu_4, l_4, L, J, K, i, \Gamma_{\text{vib}}, \Gamma_{\text{rot}}, \Gamma_{\text{tot}}$$
.

 $\nu_1, \nu_2, \nu_3, \nu_4$ correspond to the four vibrational modes. As explained above, due to the nature of the ν_2 (umbrella) mode, each vibrational level is split into a doublet. This gives rise to an inversion label i = s/a (symmetric/antisymmetric), indicating the parity under inversion through the planar configuration.

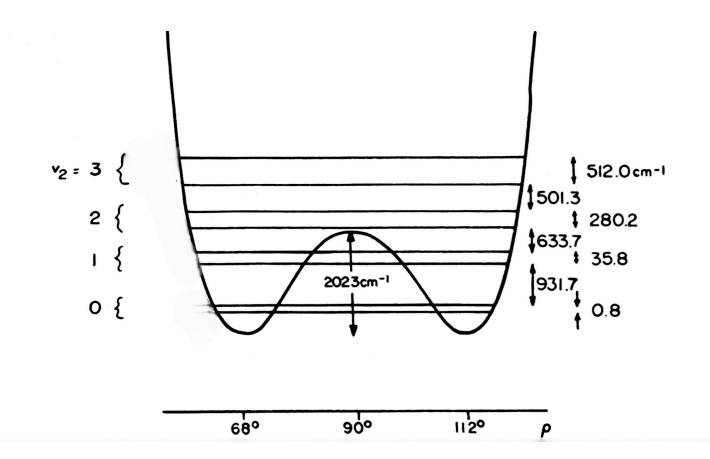


Figure 2: Inversion energy levels of NH₃. The energy level splittings are given in cm⁻¹. Molecular rotation leads to centrifugal distortion of the potential energy curve, which causes the inversion splitting to depend on the total rotational angular momentum J and its projection on the molecular symmetry axis K.

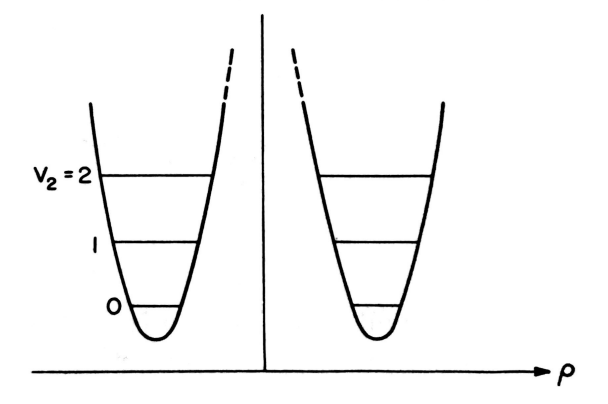


Figure 3: The potential function and umbrella vibration energy levels of a rigid C_{3v} molecule. If ammonia did not exhibit tunneling through the inversion barrier, its symmetry group would remain C_{3v} [8].

The two doubly degenerate vibrational modes, ν_3 and ν_4 , generate vibrational angular momentum described by the quantum numbers l_3 and l_4 , with allowed values:

$$l_i = -\nu_i, -\nu_i + 2, \dots, \nu_i - 2, \nu_i$$
 for $i = 3, 4$.

These arise from the 2D isotropic harmonic oscillator basis and contribute to the total vibrational angular momentum $L = |l_3 + l_4|$.

The total angular momentum quantum number is J, and its projection on the molecule-fixed z-axis is denoted by K = |k|, where $k = -J, \ldots, +J$ in integer steps.

The molecular wavefunction symmetries are labeled by Γ_{vib} , Γ_{rot} , and Γ_{tot} , corresponding to the symmetry species of the vibrational, rotational, and total internal wavefunctions in the molecular symmetry group $D_{3h}(M)$. These symmetry labels belong to the irreducible representations of $D_{3h}(M)$: A'_1 , A''_1 , A''_2 , A''_2 , E', and E'', and are essential for applying group-theoretical selection rules.

The assignment of symmetry species and angular momentum quantum numbers follows the Herzberg convention, with ν_1 and ν_2 associated with 1D harmonic oscillator functions, and the degenerate modes ν_3 and ν_4 linked to 2D isotropic harmonic oscillator wavefunctions $|\nu,l\rangle$. The total vibrational angular momentum and its symmetry determine the allowed rovibrational couplings and transitions.

A full table 4 detailing the symmetry operations and character table of $D_{3h}(M)$ is included below for reference. For a complete derivation and further details, see [8].

While these 13 quantum numbers provide a complete description of the rovibrational and inversional state of the molecule, they are often over-specified, particularly for lower-lying energy levels. Nevertheless, they are crucial for unambiguously identifying and cataloging NH₃ states in spectroscopic databases.

• General selection Rules:

The selection rules governing rovibrational transitions are dictated by the standard angular momentum and symmetry considerations of molecular spectroscopy.

Case of a Parallel Band: When the dipole moment change during a vibrational transition is aligned with the molecular symmetry axis (typically the z-axis), the band is classified as a parallel band. This is the case for the symmetric stretching (ν_1) and symmetric bending (ν_2) modes in ammonia (NH₃), where the vibration occurs along the axis of symmetry. The selection rules for parallel bands are:

$$\Delta K = 0$$
, $\Delta J = 0, \pm 1$ (but $J = 0 \rightarrow J = 0$ is forbidden)

Case of a Perpendicular Band: When the dipole moment change is perpendicular to the molecular axis, the transition is said to form a *perpendicular band*. In NH₃, this applies to the doubly degenerate bending and stretching modes ν_3 and ν_4 . The corresponding selection rules are:

$$\Delta K = \pm 1$$
, $\Delta L = \pm 1$, $\Delta J = 0, \pm 1$

K		$\Gamma_{ m rot}$
0	J even J odd	A' ₁ A' ₂
6n ± 1	j odd	E"
$6n \pm 2$		E'
6n + 3		$A''_1 + A''_2$
6n + 6		$A'_1 + A'_2$

(a) Symmetry species of the rotational states of ammonia in the $D_3h(M)$ group (n = 0; 1; 2... and $K \ge 0$)

$\begin{array}{c ccccccccccccccccccccccccccccccccccc$	$D_{3h}(M)^2$:	(123)	(23)	E*	(123)*	(23)*
A_1' : 1 1 1 1 1 1 1 1 1 1 A_2' : 1 1 -1 1 1 1 -1 A_2' : 1 1 -1 0 2 -1 0 A_1'' : 1 1 1 -1 -1 -1 1 1	D_{3h} : E	$2C_3$	$3C_2$	$\sigma_{ extbf{h}}$	2S ₃	$3\sigma_{\rm v}$
A_2' : 1 1 -1 1 1 -1 E': 2 -1 0 2 -1 0 A'': 1 1 1 -1 -1 -1 A'': 1 1 -1 -1 1	Equiv. rot.: R ⁰	$R_z^{2\pi/3}$	R_0^*	R _z *	$R_z^{-\pi/3}$	$R_{\pi/2}^{\pi}$
E': 2 -1 0 2 -1 0 A'' : 1 1 1 -1 -1 -1 1	A ₁ ': 1	1	1	1	1	1
A_1'' : 1 1 1 -1 -1 -1 A_2'' : 1 1 -1 -1 1	A_2' : 1	1	-1	1	1	-1
A_2'' : 1 1 -1 -1 1	E': 2	-1	0	2	-1	0
-	A": 1	1	1	-1	-1	-1
E": 2 -1 0 -2 1 0	A": 1	1	-1	-1	-1	1
	E": 2	-1	0	-2	1	0
	A": 1	1 1 -1	-1 0		-	1 1 1

Figure 4: Symmetry operations and characters of the $D_3h(M)$ Molecular symmetry group.

These selection rules also stem from the general requirement that the transition dipole moment matrix element must be non-zero:

$$\langle \phi'_{\text{int}} | \mu_A | \phi''_{\text{int}} \rangle \neq 0, \quad A = X, Y, Z$$

where ϕ_{int} is the rovibrational–inversion eigenfunction of the molecule. This condition reflects the parity and symmetry constraints imposed by the molecular symmetry group, here $D_{3h}(M)$ for ammonia, and ensures that only transitions consistent with the overall symmetry properties of the wavefunctions are spectroscopically allowed.

4 Probing Variations in μ : Overview of Current Work

Radio telescopes offer high-resolution observations of deep space and our galaxy in the microwave (MW) and millimeter-wave (MMW) spectral regions. Maser emission lines [10] and absorption lines from cold, collisionless galactic [11] and extragalactic [12] molecular clouds exhibit linewidths as narrow as ~ 100 kHz, leading to frequency uncertainties of just a few kilohertz.

Although stable MW/MMW sources exist, laboratory data quality is limited by spectrometer accuracy [10, 11, 12],. Additionally, key reference databases (HITRAN, JPL, CDMS, NIST) often lack frequency metrology and SI-traceability. The

best current constraints on μ -variation come from comparisons of a few methanol transitions, but these are limited by ~ 10 kHz inaccuracies in lab data.

Spatio-temporal variations in the proton-to-electron mass ratio μ can be probed using ultra-precise spectroscopic experiments, as atomic and molecular energy levels depend on μ . Two main strategies exist:

- (i) Time variation in the present epoch: This approach compares transitions with different sensitivity coefficients $T_{u,l}$ using frequency metrology across several years. The most stringent constraint so far, $|\Delta \mu/\mu| \sim 10^{-17} \text{ yr}^{-1}$, was derived from Yb⁺ optical clocks compared to caesium fountains [13]. Molecular systems like SF₆ [14] and KRb [15] also provide limits around 10^{-14} yr^{-1} .
- (ii) Cosmological variation: This method compares molecular transition frequencies in distant astrophysical sources to laboratory measurements. It is the main goal of the ULTIμOS project. Molecules such as methanol (CH₃OH) and ammonia (NH₃), with tunneling motions (inversion in NH₃, internal rotation in CH₃OH), yield transitions with strong sensitivity to μ-variation in the MW/MMW domain.

Observations of molecular absorbers at redshifts $z \sim 0.7$ –0.9 place limits of $|\Delta \mu/\mu| < 3.6 \times 10^{-7}$ at 3σ , corresponding to look-back times of half the Universe's age. Assuming linear variation, this equates to a limit of $\sim 10^{-17} \text{ yr}^{-1}$.

Methanol and ammonia are also used to study μ -variation within the Milky Way. Narrow linewidths ($\sim 10 \, \text{kHz}$) and high SNRs permit central frequency uncertainties down to $\sim 100 \, \text{Hz}$. However, methanol-based constraints are currently limited by lab frequency accuracy (1–10 kHz). As Daprà et al. put it, "it is clear that the observations [...] are more accurate than most experimental data from the laboratory" [11].

Unlike CH₃OH, the NH₃ method [16] relies on the well-known ¹⁴NH₃ inversion transition (J = 1, K = 1), which has a sensitivity coefficient of $T_{u,l} \approx -4.4$ and an associated uncertainty of approximately 60 Hz. This method typically involves comparing the inversion line to **co-spatial rotational transitions** of other molecules, potentially introducing systematic biases. In contrast, methanol (CH₃OH) transitions avoid this issue by providing multiple lines with different $T_{u,l}$ values, allowing comparisons within the same molecule and enabling self-contained and internally consistent analyses.

Many other transitions with enhanced sensitivity to μ have also been identified. In methanol, for example, certain isotopologues yield $T_{u,l}$ values up to ten times higher ($-88 \le T_{u,l} \le 330$) [17, 18]. Transitions in excited vibrational states of ¹⁴NH₃ and ¹⁵NH₃ (e.g., ν_2 , ν_4 , $2\nu_2$) have also been identified, with sensitivity coefficients reaching $T_{u,l} \sim 1000$ or higher [5, 6, 7, 19]. When combined with the NH₃(1,1) line, these transitions could offer internal constraints on μ -variation, thereby avoiding cross-species comparison errors. However, such analyses require highly accurate ab initio calculations of $T_{u,l}$, supported by precision laboratory frequency metrology.

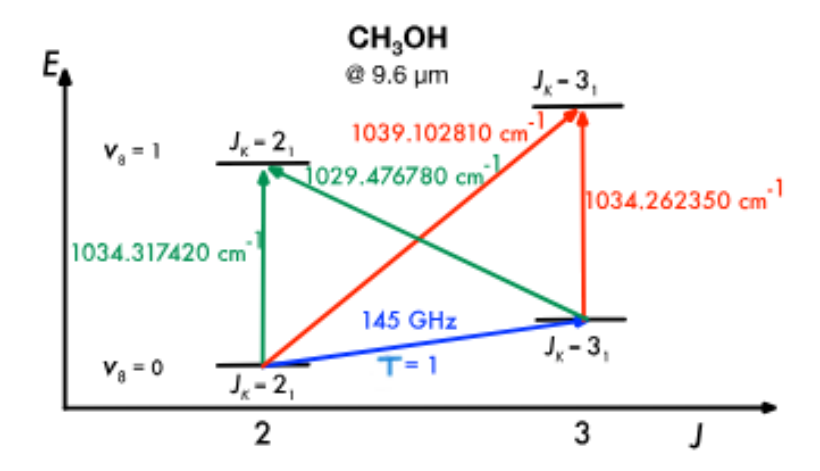


Figure 5: Illustration of the measurement method. The blue arrow represents a methanol MW transition that has been observed and used to constrain variations of μ [11]. The current laboratory data on this transition limit the corresponding constraints on $\Delta\mu/\mu$. The red and green arrows indicate MIR transitions at 9.6 μ m belonging to the ν_8 C–O stretch vibrational mode. These transitions can be combined to determine the MW transition shown.

5 Indirect Determination of MW/MMW Transitions via MIR Spectroscopy

5.1 Original Approach

We propose an original approach illustrated in Fig.5 instead of directly carrying out MW/MMW spectroscopy (blue arrow in Fig.5), we suggest determining the relevant MW/MMW transition intervals indirectly, through differences or more elaborate combinations of MIR transition frequencies (red or green arrows in Fig.5.

The blue arrow represents a MW transition at 145 GHz in Methanol with a sensitivity coefficient T=1. It has been detected in a dense dark cloud core in the Milky Way and used to constrain μ variations [11], with current laboratory data limiting the corresponding constraint. The red and green arrows indicate MIR transitions around 9.6 μ m, belonging to the ν_8 C–O stretch vibrational mode listed in the HITRAN database. According to Fig.5, the MW transition can be retrieved from combinations of MIR transitions—specifically, the difference of either the green or red MIR transitions.

Our goal was to apply this idea to ammonia (NH₃), searching for such possibilities in the HITRAN database.

5.2 Strategy for Identifying Transition Combinations in Ammonia

I developed a Python code to search for combinations of transitions sharing common energy levels by comparing their quantum numbers. The logic can be broken down into two main schemes:

1. Three-Level System with Two Transitions see Fig.6a:

- (1) Both transitions must have frequencies between 700 and 1700 cm⁻¹ (\approx 6–14 μ m) to ensure MIR coverage, which allows precise measurements using tunable quantum cascade lasers.
- (2) Each transition must have an intensity > 10^{-21} cm⁻¹/molecule·cm⁻²(For pure isotope). This threshold ensures that I am selecting intense, and thus likely allowed, transitions.
- (3) The difference in frequency $|\nu_i \nu_j|$ must lie in the MW/MMW domain $(0\text{--}10 \text{ cm}^{-1})$, to match the targeted range.
- (4) The four states involved (2 initial and 2 final) in both transitions must correspond to only three unique energy levels, ensuring the formation of a true three-level system.

2. Four-Level System with Three Transitions see Fig.6b:

- (1) Each transition must again fall in the 700–1700 cm⁻¹ range.
- (2) Each must have intensity $> 10^{-21}$ cm⁻¹/molecule·cm⁻².
- (3) The combination $|\nu_i + \nu_j \nu_k|$ must be within the MMW/MW range (0–10 cm⁻¹), capturing a transition generated through a combination of the three MIR transitions.
- (4) The six states involved across the three transitions must reduce to four unique energy levels, ensuring coherence in the constructed four-level scheme.

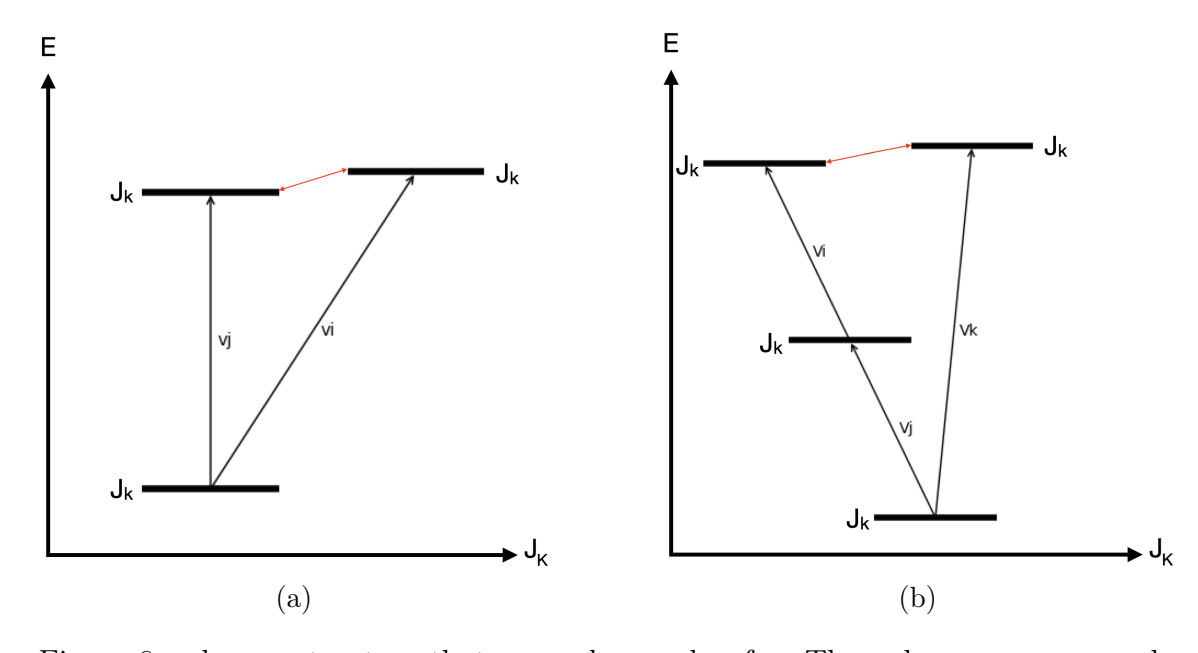


Figure 6: schemes structure that my code searches for. The red arrow corresponds to the MMW/MW transition.

This approach allows identifying potential MW/MMW transitions indirectly, using MIR spectroscopy data available in HITRAN. It forms the basis for extending μ -variation studies to systems such as ammonia using existing laboratory techniques.

6 Results and Analysis

Using the Python script described previously, I obtained a set of transition combinations and schemes that satisfy the defined criteria for $^{14}NH_3$. For the **three-level system**, under the constraints that both MIR transitions must lie between 700 and 1700 cm⁻¹ and have an intensity greater than 1×10^{-21} cm⁻¹/molecule·cm⁻², a total of **9 schemes** were identified.

Similarly, for the **four-level system**, applying the same frequency and intensity criteria, **16 schemes** were found.

The next crucial task was to identify which of these schemes are more promising. Two main criteria determine the relevance of a scheme:

1. The sensitivity coefficient T of the resulting MW/MMW transition: This coefficient characterizes how sensitive a given transition is to variations in the proton-to-electron mass ratio μ . The higher the value of T, the more suitable the transition is for probing μ -variation. However, calculating this coefficient is a complex task that generally cannot be reliably performed without advanced theoretical tools. Therefore, I rely on previously published work in the literature where such sensitivity coefficients have been calculated for ammonia transitions.

2. Astrophysical observability:

The usefulness of a given MW/MMW transition also depends on whether it has been detected in astrophysical environments, such as in interstellar clouds. While databases like Splatalogue aggregate information from resources like the Cologne Database for Molecular Spectroscopy (CDMS), the JPL Molecular Spectroscopy Database, and the Lovas/NIST catalogue and others..., they are incomplete and, in many cases, outdated (last major updates around 2016). For this reason, I turned to a literature search to identify papers reporting the observation of ammonia lines. Some of these lines are not helpful for our purposes as I will explain later.

6.1 Candidate Transition Schemes for Probing μ-variation

Example: Among the extracted schemes, one involves a well-known ground-state inversion transition, specifically the $J_K^{\pm} = 3_3^{\pm}$ line of ammonia. This transition, illustrated in Fig.7, is connected via a possible combination of MIR transitions within the HITRAN database.

What makes this scheme noteworthy is that the corresponding microwave transition has indeed been observed in astrophysical environments. In ref:[20], the authors report the detection of the $3_3^+ \rightarrow 3_3^-$ inversion line of NH₃ with a high signal-to-noise ratio, with + and - denoting symmetric and antisymmetric Vibration-Inversion

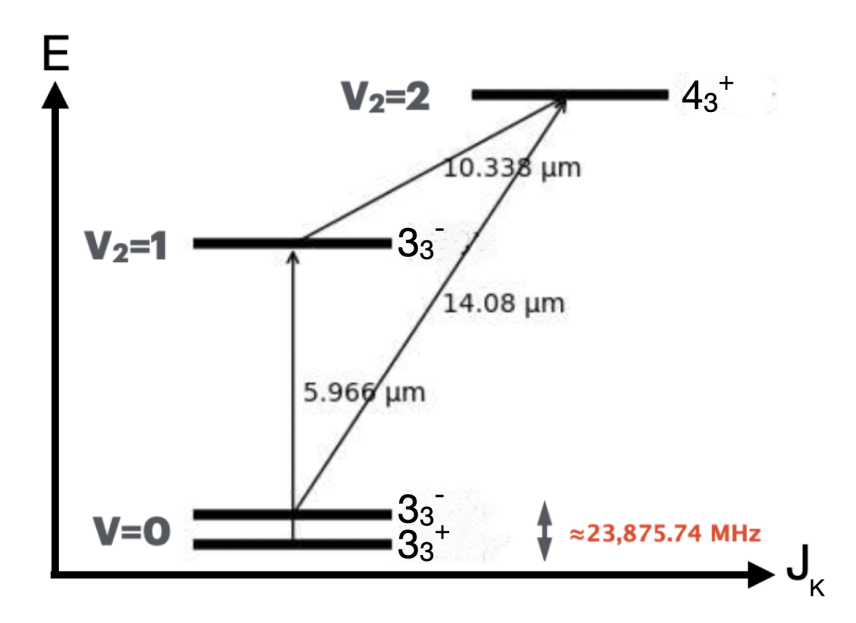


Figure 7: The targeted transition is the vibrational ground state(v=0) MW inversion transition.

states, respectively. The frequency targeted in their observation was 23,870.1292 MHz. By comparison, the HITRAN database lists the experimental frequency as 23,875.74 MHz. This small discrepancy can be attributed to known uncertainties in both astrophysical and laboratory measurements.

Despite this strong astrophysical and laboratory support, I ultimately consider this scheme not beneficial for the goals of our study. Ground-state inversion transitions of ammonia are very well known and have already been extensively characterized in laboratory settings. Moreover, their sensitivity coefficient T to variations in the proton-to-electron mass ratio μ is approximately 4.4, which, while non-negligible, is standard for such transitions and offers limited added value for new tests of fundamental physics. As a result, this scheme does not represent a promising candidate for further exploration in our context.

• Schemes Involving Highly Sensitive $2\nu_2 \rightarrow \nu_4$ Transitions

I also identified three particularly interesting schemes (see Figs. 9a, 9b, and 9c) that include microwave transitions with high sensitivity coefficients. These transitions occur between the $2\nu_2$ and ν_4 rotation-vibration energy levels of ammonia, where the $2\nu_2$ state corresponds to ($\nu_2=2,\ \nu_1=\nu_3=\nu_4=0$) and the ν_4 state corresponds to ($\nu_4=1,\ \nu_1=\nu_2=\nu_3=0$), which are known to exhibit numerous accidental near-degeneracies see fig:8 . Such near-degeneracies, arising from strong Coriolis interactions between the two states [21], lead to transitions with significantly enhanced sensitivity to variations in the proton-to-electron mass ratio μ since the sensitivity T is inversely proportional to the difference of energy between the levels involved see eq:(1).

One surprising example, as reported in Ref. [19], features a transition with a sensitivity coefficient as high as T = -16738. This transition corresponds to the 5_3^+ (ν_4) $\leftarrow 5_2^+$ ($2\nu_2$) rovibrational line. Although this particular transition

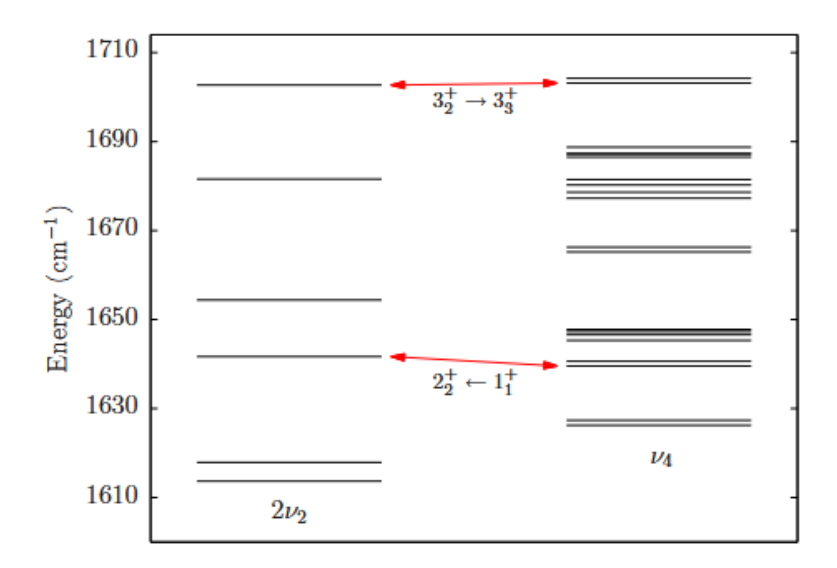


Figure 8: Accidental near-degeneracies between the $2\nu_2$ and ν_4 rotation-vibration energy levels of ammonia. Energy levels are labeled as J_K^{\pm} . [19]

is extremely weak, it demonstrates the dramatic enhancement in sensitivity that can result from the mixing of nearly degenerate states. A number of these transitions between $2\nu_2$ and ν_4 have also been measured experimentally [22, 23], and a comprehensive list of calculated sensitivity coefficients is available in the work of Spirko and Owen (2016) [19], reproduced in Table (10).

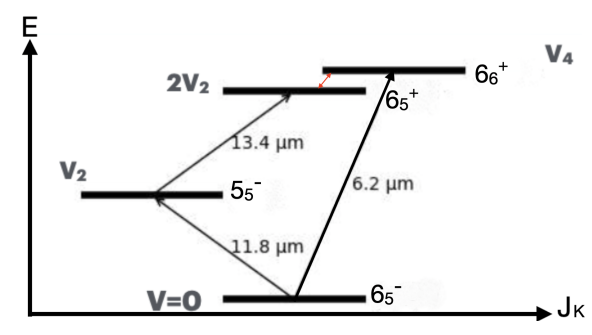
Among the results from my Python-based search algorithm, three of the schemes included transitions listed in this table (highlighted with underlining in Table (10)). This overlap confirms the relevance of our approach in identifying spectroscopically interesting schemes for probing variations in μ .

However, these transitions come with certain challenges. To our knowledge, none of them have yet been observed in astrophysical environments, likely due to the high excitation levels involved. Such transitions may require specific astrophysical environments for population. The difficulty is in finding suitable astrophysical sources and resolving their spectra with sufficient precision. Additionally, reproducing these schemes in the laboratory may be technically demanding due to the need to excite multiple transitions at different frequencies. This would require the use of several laser sources operating at distinct wavelengths. Nevertheless, such an experimental implementation remains feasible, particularly with the development of advanced laser systems such as quantum cascade lasers.

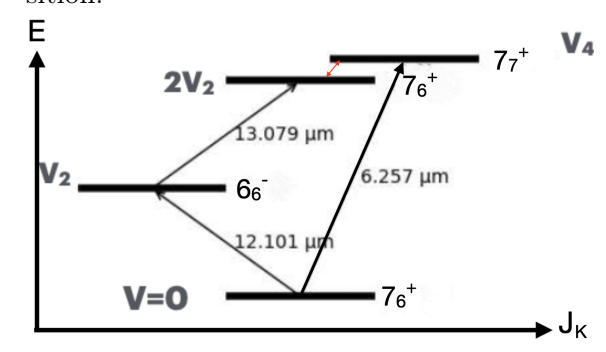
Despite these limitations, the high sensitivity of these transitions makes them compelling candidates for future investigation, both in the laboratory and in astrophysical searches.

• Inversion transition in the ν_2 band:

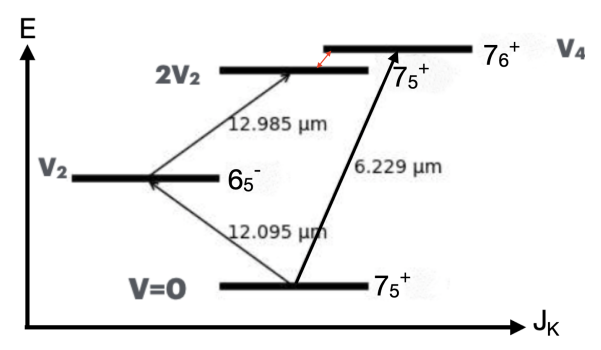
One of the most promising candidates identified involves an inversion transition within the ν_2 vibrational band. As reported in Ref:[6], the ν_2 band of



(a) Candidate Scheme for $6_5^+ \rightarrow 6_6^+$ MW transition.



(b) Candidate Scheme for $7_6^+ \rightarrow 7_7^+$ MW transition.



(c) Candidate Scheme for $7_5^+ \rightarrow 7_6^+$ MW transition.

Figure 9: Schemes Involving Highly Sensitive $2\nu_2 \rightarrow \nu_4$ Transitions.

ammonia exhibits accidental coincidences between ro-inversional states with significant dependence on centrifugal distortion effects. These effects are especially prominent in the case of $\Delta K = \pm 3$ "forbidden" transitions, such as 3_3^- and 3_0^+ within the ν_2 band. Jansen et al. [5] and Flambaum & Kozlov [16] calculated a sensitivity coefficient of T = -938, which is among the highest known and highlights this transition as a particularly compelling probe for variations in the proton-to-electron mass ratio μ .

Interestingly, this scheme was also retrieved using my code see Fig.(11), showing its experimental viability. Notably, the transition from 3_3^+ in the ground state to 3_3^- in the ν_2 band is allowed by the standard selection rules and has an experimental intensity on the order of $10^{-19} \, \mathrm{cm}^{-1}/(\mathrm{molecule \cdot cm}^{-2})$, which

$v' \leftarrow v''$	$J_K^{\pm}{}' \leftarrow J_K^{\pm}{}''$	ν _{expt} (MHz)	$A (s^{-1})$	T	$v' \leftarrow v''$	$J_K^{\pm}{}' \leftarrow J_K^{\pm}{}''$	ν _{expt} (MHz)	$A (s^{-1})$	T
$v_4 \leftarrow 2v_2$	$0_0^+ \leftarrow 1_1^+$	379 596.5	4.703×10^{-6}	- 18.70	$v_4 \leftarrow 2v_2$	$5_4^+ \leftarrow 5_3^+$	434 941.1	9.782×10^{-5}	- 15.59
$v_4 \leftarrow 2v_2$	$1_1^+ \leftarrow 1_0^+$	824 624.2	6.427×10^{-5}	-9.13	$v_4 \leftarrow 2v_2$	$5_3^+ \leftarrow 5_2^+$	527 333.3	8.219×10^{-5}	-13.31
$2\nu_2 \leftarrow \nu_4$	$2_1^+ \leftarrow 1_0^+$	231 528.2	1.180×10^{-6}	27.91	$\nu_4 \leftarrow 2\nu_2$	$5_2^+ \leftarrow 5_1^+$	618 776.8	4.583×10^{-5}	-11.66
$v_4 \leftarrow 2v_2$	$2_{2}^{+} \leftarrow 2_{1}^{+}$	687 852.5	6.318×10^{-5}	- 10.70	$v_4 \leftarrow 2v_2$	$5_1^+ \leftarrow 5_0^+$	672 376.5	2.542×10^{-5}	-10.86
$2\nu_2 \leftarrow \nu_4$	$3_3^+ \leftarrow 2_2^+$	489 672.2	4.360×10^{-6}	12.72	$v_4 \leftarrow 2v_2$	$6_6^+ \leftarrow 6_5^+$	261 535.4	5.745×10^{-5}	-23.29
$v_4 \leftarrow 2v_2$	$3_3^+ \leftarrow 3_2^+$	557 275.3	7.623×10^{-5}	- 12.87	$v_4 \leftarrow 2v_2$	$6_5^+ \leftarrow 6_4^+$	340 322.9	9.137×10^{-5}	-18.52
	$3_3^+ \leftarrow 3_2^+$ $3_2^+ \leftarrow 2_1^+$	672 644.4	3.223×10^{-5}	8.89	$v_4 \leftarrow 2v_2$	$6_4^+ \leftarrow 6_3^+$	413 748.1	9.006×10^{-5}	-15.98
$2\nu_2 \leftarrow \nu_4$	2 1				$v_4 \leftarrow 2v_2$	$6_3^+ \leftarrow 6_2^+$	488 661.3	6.308×10^{-5}	-14.12
$v_4 \leftarrow 2v_2$	$3_2^+ \leftarrow 3_1^+$	679 163.4	6.964×10^{-5}	- 10.79	$v_4 \leftarrow 2v_2$	$6_2^+ \leftarrow 6_1^+$	559 214.0	3.027×10^{-5}	-12.73
$v_4 \leftarrow 2v_2$	$3_1^+ \leftarrow 3_0^+$	774 889.5	4.660×10^{-5}	-9.59	$v_4 \leftarrow 2v_2$	$7_7^+ \leftarrow 7_6^+$	198 997.4	4.284×10^{-5}	-27.24
$2\nu_2 \leftarrow \nu_4$	$3_1^+ \leftarrow 2_0^+$	842 667.6	1.210×10^{-4}	6.91	$v_4 \leftarrow 2v_2$	$7_6^+ \leftarrow 7_5^+$	266 541.0	7.700×10^{-5}	- 21.20
$v_4 \leftarrow 2v_2$	$4_4^+ \leftarrow 4_3^+$	441 874.1	7.796×10^{-5}	-15.68	$v_4 \leftarrow 2v_2$	$7_5^+ \leftarrow 7_4^+$	321 935.0	8.437×10^{-5}	-18.62
$v_4 \leftarrow 2v_2$	$4_3^+ \leftarrow 4_2^+$	548 781.8	9.102×10^{-5}	-12.94	$v_4 \leftarrow 2v_2$	$7_4^+ \leftarrow 7_3^+$	375 174.5	6.887×10^{-5}	-16.99
$v_4 \leftarrow 2v_2$	$4_2^+ \leftarrow 4_1^+$	657 787.0	6.078×10^{-5}	-11.07	$v_4 \leftarrow 2v_2$	$7_3^+ \leftarrow 7_2^+$	430 468.6	4.113×10^{-5}	-15.29
$v_4 \leftarrow 2v_2$	$5_5^+ \leftarrow 5_4^+$	342 797.1	7.054×10^{-5}	-19.22	$v_4 \leftarrow 2v_2$	$8_8^+ \leftarrow 8_7^+$	154 415.5	3.036×10^{-5}	-30.19

Figure 10: Astronomically relevant transitions between the $2\nu_2 \leftrightarrow \nu_4$ vibrational states of NH3,table from ref:[19], A: Einstein coefficient, where intensity $I \propto A$ (s⁻¹)

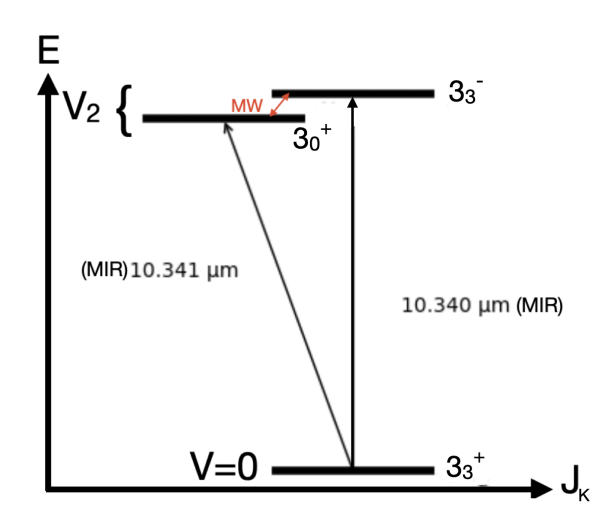


Figure 11: Vibration–rotation–inversion levels of ¹⁴NH₃ in the ν_2 vibrational band, with mid-infrared (MIR) transitions connecting these levels to the ground state. Also shown is the microwave (MW) transition $3_3^- \rightarrow 3_0^+$ (2.884 GHz) within the ν_2 band, which exhibits extraordinarily high sensitivity, T=-938.

is relatively strong. On the other hand, the transition from 3_3^+ in the ground state to 3_0^+ in the ν_2 band is formally forbidden due to $\Delta K = \pm 3$, yet surprisingly, it also exhibits a similar high intensity, on the same order of magnitude.

This apparent violation of the $\Delta K=0$ selection rule is explained by the strong mixing between closely spaced rotational levels within the ν_2 vibrational state. This mixing allows "forbidden" transitions such as $\Delta K=\pm 3$ to gain significant intensity, making them observable.

From an experimental perspective, a feasible approach would be to measure both MIR transitions— $\nu=0:3_3^+\to\nu_2:3_3^-$ and $\nu=0:3_3^+\to\nu_2:3_0^+$ —with high precision in the laboratory (few Hz). The frequency difference between these two MIR transitions corresponds to the MW transition $(3,3)^-\to (3,0)^+$ within the ν_2 band, which has extraordinarily high sensitivity. While this MW transition has not yet been detected astrophysically, Špirko and others have noted that transitions with comparable Einstein coefficients ($A\sim 10^{-1}$ to $10^{-2}~{\rm s}^{-1}$) have been observed, suggesting that such a detection could be feasible in the near future.

If this MW transition were to be observed astrophysically, it would offer a powerful new test of the constancy of the proton-to-electron mass ratio. Its extreme sensitivity would enable a truly decisive test of fundamental physics beyond the Standard Model.

• Astrophysically Observed Inversion Transition in the ν_2 Band

After conducting a bibliographic study, I identified two microwave inversion-rotation transitions within the ν_2 vibrational band of ammonia that have been observed in astrophysical environments and also reported in one of Spirko's papers [6]. These transitions are accompanied by calculated sensitivity coefficients: one is the $2_1^+ \to 1_1^-$ transition, with a sensitivity T=16.92, and the other is the $0_0^- \to 1_0^+$ transition, with T=-6.409. Both occur within the ν_2 band.

To further exploit these transitions for μ -variation studies, I manually searched for mid-infrared (MIR) transitions that connect either of the upper or lower states of these MW transitions to levels in the ground state (GS). For the $2_1^+ \to 1_1^-$ transition, I found four possible MIR schemes that satisfy this criterion. Among them, I selected the two most promising candidates, presented in Fig. 12.

As illustrated, both the 2_1^+ and 1_1^- levels are connected via strong MIR transitions to different ground state levels, one of which is the well-known 1_1^{\pm} pure inversion transition. The frequency of this GS transition is very well measured (\sim 60 Hz uncertainty) and characterized in the literature, which allows us to fix its frequency and focus on precise MIR spectroscopy to determine the frequencies of the other two transitions leading to the ν_2 levels.

Interestingly, the $2_1^+ \rightarrow 1_1^-$ MW transition has been observed in our own galaxy—specifically in the Sgr B2(N) molecular cloud—using the IRAM 30-meter telescope. Since the source lies within the Milky Way, its redshift is

effectively zero ($z \approx 0$). This makes it unsuitable for measuring the temporal evolution of the proton-to-electron mass ratio μ , but very promising for probing potential spatial variation in μ across galactic environments. Additionally, its proximity provides high spectral resolution, which is advantageous for accurate frequency measurements.

In Fig. 12b, I present another viable scheme linking the same MW transition but using a different ground state level, also considered a promising candidate. Upon discussing this with the spectroscopy team at LPL, I learned that they were already aware of this transition and had previously measured the MIR transition from v = 0, 1^-_1 to ν_2 , 2^+_1 with an accuracy of approximately 10 kHz. They expressed confidence that with current techniques, a much higher precision can be achieved. Furthermore, they have also performed MMW spectroscopy of the direct $2^+_1 \rightarrow 1^-_1$ transition using a 0.14 THz field, obtaining a transition frequency accuracy on the order of 1 kHz.

As for the second transition $0_0^- \to 1_0^+$ in the ν_2 band, I found no viable MIR transitions connecting either state to the ground state. Combined with its relatively lower sensitivity coefficient, this transition is therefore less promising for our purposes.

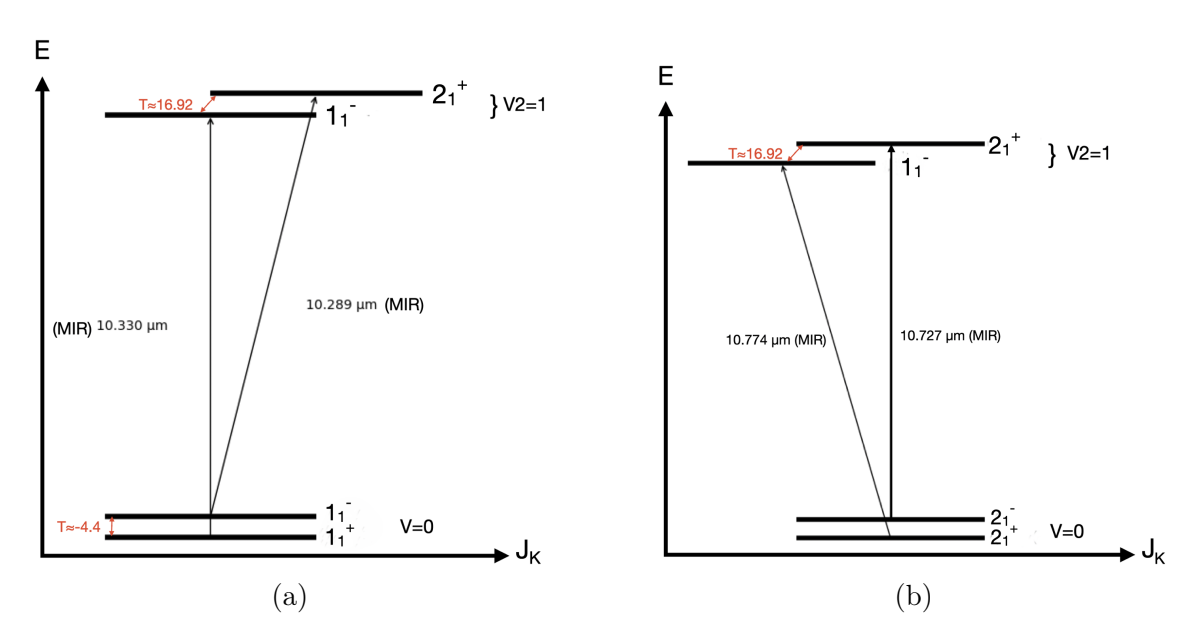


Figure 12: schemes containing the observed MW transition extra-terrestrially.

6.2 Conclusion

Following our recent meeting with the MONARIS laboratory (Christof Janssen), the LPL team (Benoît Darquié), and our group, we discussed the various spectroscopic schemes and transitions identified so far. While several promising candidates have emerged—including highly sensitive transitions such as the forbidden $3_3^- \rightarrow 3_0^+$ (2.884 GHz) inversion transition within the ν_2 band—our main bottleneck remains the lack of confirmed extraterrestrial observations for many of these lines.

As a result, we concluded that it is now essential to establish communication with astrophysicists or astronomers. Their expertise is crucial for evaluating the observational feasibility of these transitions. For instance, we need to understand whether transitions like the aforementioned forbidden one could realistically be detected with current or upcoming astronomical instrumentation. Additionally, we seek insight into the possibility of observing $2\nu_2 \to \nu_4$ transitions, which are also of great interest due to their high sensitivities.

Key questions include:

- What is the current observational status of these transitions in astrophysical environments?
- Are there ongoing efforts or planned campaigns targeting such lines?
- What are the limitations and capabilities of current telescopes and detection technologies?
- Is there a comprehensive and up-to-date database compiling molecular line observations, and if so, where can it be accessed?

7 Optical Signal Stabilization

7.1 Importance

High-resolution spectroscopy requires lasers with exceptional frequency stability and accuracy. Several specialized laboratories, such as LTE (former SYRTE) ¹, provide ultra-stable laser sources. For instance, LTE produces an infrared signal at 1542 nm with a relative stability better than 10⁻¹⁴ over all time scales. These signals are distributed to other laboratories through dedicated optical fiber networks, notably the REFIMEVE infrastructure, to serve as frequency references for local laser systems.

However, optical fiber links between laboratories are susceptible to environmental perturbations—such as temperature fluctuations, mechanical vibrations, and pressure variations—which induce changes in the optical path length. These variations introduce phase noise that degrades the stability of the transmitted signal.

To mitigate this, phase noise compensation systems are employed. REFIMEVE, for example, implements such noise cancellation techniques extensively to ensure reliable signal transfer. At Laboratoire Kastler Brossel (LKB), the REFIMEVE signal serves as a reference for a frequency comb used in precision experiments, including trapped-ion spectroscopy and, notably, my upcoming spectroscopy of ¹⁴NH₃.

While the REFIMEVE signal is actively stabilized between LTE and the extraction point at LKB, approximately 200 meters of optical fiber remain uncorrected between the extraction point and the experimental setup using the frequency comb. This uncorrected segment presents a significant source of potential phase noise, which must be carefully managed to preserve the overall signal integrity.

¹Systèmes de Référence Temps-Espace

7.2 Protocol Used for Stabilization and Experimental Setup

The protocol implemented to compensate for phase noise in the optical fiber is inspired by the method proposed by Long-Sheng Ma, Peter Jungner, Jun Ye, and John L. Hall [24]. The experimental setup used is shown in Fig. 13. The setup was implemented by two interns in February 2025.

We begin with a 1542 nm laser source whose output passes through an optical isolator to prevent detrimental back-reflections. The laser used is a fiber laser from NKT Photonics, model $Koheras\ Basik$, chosen to work close to the REFIMEVE signal wavelength. It is tunable for only ± 0.5 nm and delivers up to 27 dBm (500 mW) of optical power. The beam is then split at point A by a 90/10 fiber beam splitter: 10% of the light is directed into a short arm (phase reference) and reflected back by a Faraday mirror (FM), while the remaining 90% continues to point E, where it passes through an acousto-optic modulator (AOM) that shifts the frequency by 80 MHz.

After the AOM, the beam travels a 215-meter-long optical fiber to the far end of the link. There, it reaches another 90/10 splitter: 90% of the light continues toward the user (and is effectively lost for feedback), while the remaining 10% is reflected back by a second Faraday mirror. This reflected signal retraces the same 215 m fiber path and passes again through the AOM, receiving a second 80 MHz shift, for a total of 160 MHz.

This 160 MHz shifted signal recombines at the initial 90/10 splitter (point A) with the 10% signal returned from the short arm. These two beams interfere and are detected by a photodiode, which converts the optical beat signal into an electrical signal centered at 160 MHz.

The beatnote can be directly monitored using a spectrum analyzer by extracting the signal through the power splitter (PS). It is then amplified by 40 dB (via two ZFL-500LN+ amplifiers), filtered using a bandpass filter centered at 160 MHz to eliminate unwanted spectral components, and then divided by 8 to produce a 20 MHz signal.

This 20 MHz signal is compared in a phase-frequency detector (PFD) with a stable 20 MHz reference generated by a dual waveform generator that also delivers the 80 MHz with phase coherence between the 80 MHz and 20 MHz. This generator itself is synchronized to a 10 MHz quartz oscillator serving as a unified frequency reference.

The PFD produces an error signal representing the phase difference between the beatnote and the reference. This error signal is used in a feedback loop to modulate the 80 MHz output of the waveform generator that drives the AOM. In this way, a phase-locked loop (PLL) is established, dynamically compensating for phase noise induced by fluctuations in the optical path length. The error signal can also be monitored on an oscilloscope to evaluate loop performance.

It is important to note that the entire system is fiber-based; no free-space optics or manual beam alignment is required. All optical paths are implemented using standard single-mode optical fibers with FC-APC connectors, ensuring optimal mode purity.

Mathematical description of the compensation process:

Let the optical signal emitted by the laser be:

$$E_i(t) = E_0 \cos(\omega_L t + \phi)$$

This signal enters a Michelson-type interferometer. In the short arm, the signal is reflected back almost immediately by a Faraday mirror. If we denote the one-way phase induced by the short arm fiber as φ_{sp} , and the common path phase as φ_c , the returning signal amplitude just before the photodiode is:

$$E_{sp} = rtE_0 \cos(\omega_L t + 2\varphi_{sp} + \varphi_c + \phi)$$

Here, $r = \sqrt{0.1}$ and $t = \sqrt{0.9}$ are the reflection and transmission coefficients of the fiber couplers.

In the long arm, the light first passes through the AOM, which imparts a frequency shift Ω_{AOM} and a phase shift φ_{AOM} (see Appendix). The signal then travels a long fiber path with one-way phase φ_{Lp} . On reflection and return, it passes the AOM again. The total returning field is then:

$$E_{Lp}(t) = rt^2 E_0 \cos[(\omega_L + 2\Omega_{AOM})t + 2\varphi_{AOM} + 2\varphi_{Lp} + \phi]$$

Including the common phase φ_c , the signal arriving at the photodiode becomes:

$$B(t) = r^2 t^2 E_0 \cos[(\omega_L + 2\Omega_{AOM})t + 2\varphi_{AOM} + 2\varphi_{Lp} + \varphi_c + \phi]$$

The beat signal at the photodiode, resulting from the interference between the long and short arm returns, is:

$$s_{\text{beat}}(t) = S_b \cos[2\Omega_{\text{AOM}}t + 2\varphi_{Lp}]$$

where φ_{Lp} is the phase that needs to be compensated, and S_b is the beat signal amplitude (see Appendix). This signal is filtered and divided by 8, then sent into the PFD for phase comparison with a 20 MHz reference.

The PFD produces a phase error:

$$\varphi_{\rm error} = \varphi_{\rm beat} - \varphi_{\rm ref}$$

This phase error is converted into a voltage and used to adjust the synthesizer output that drives the AOM:

$$f(t) = f_c + G_{\text{PLL}} \cdot \varphi_{\text{error}}(t)$$

where $f_c = 80 \,\text{MHz}$ is the center frequency and G_{PLL} is the loop gain (in kHz/V). The loop thus continuously adjusts the AOM drive frequency to counteract the accumulated phase noise in the long fiber.

Further technical details regarding the AOM, Faraday mirror, and photodiode operation can be found in the Appendix.

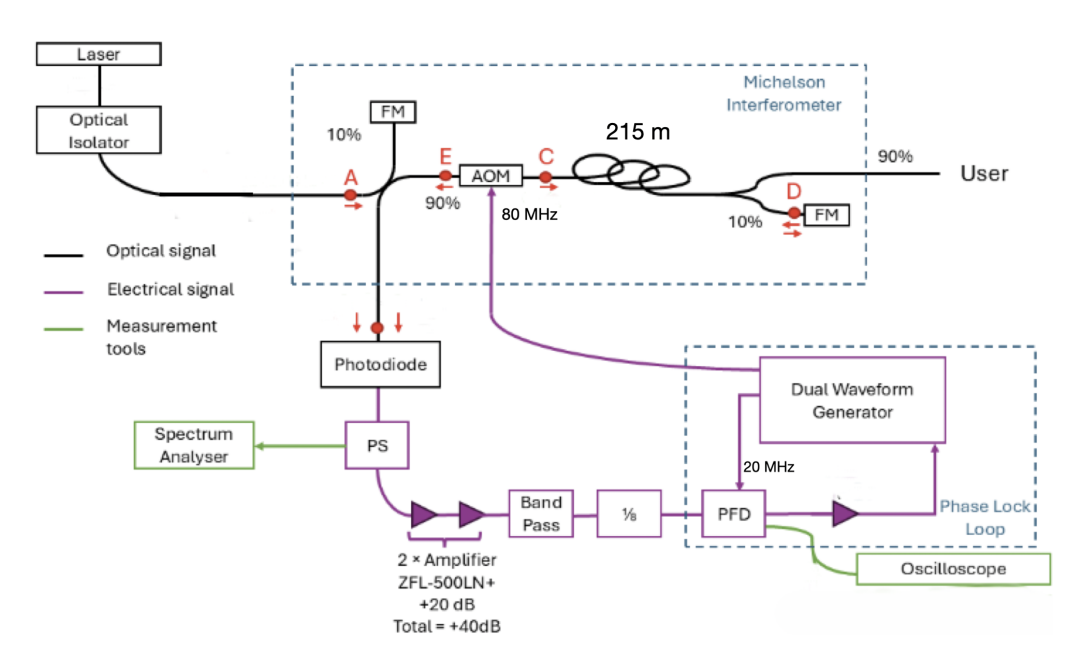


Figure 13: Phase noise compensation setup used for optical signal stabilization.

7.3 Stabilization Test and Results

To verify that the phase lock was functioning properly, we monitored the error signal on the oscilloscope. The signal remained consistently close to zero, indicating that the feedback loop was stable and that the lock was operating correctly. However, this observation alone does not provide information about the stability of the correction system, nor does it quantify how well the phase noise is being suppressed.

To assess the system's performance more rigorously, I implemented a second, independent phase noise compensation channel. This second channel will also be necessary in the future, as several teams at LKB and in the MONARIS lab intend to use stabilized REFIMEVE signals for their experiments. Both channels were fed from the same laser source by splitting the original beam into two paths: one entering Channel 1 (with 215 meters of optical fiber) and the other entering Channel 2 (where I introduced only 15 meters of fiber to simulate a short-distance transmission). To evaluate the phase stability between the two independently stabilized outputs, I directed the two output beams (from the end-user sides of each channel) to a 50/50 fiber coupler. Importantly, the driving frequencies of the two AOMs were deliberately offset: Channel 1 was driven at 80.001 MHz, and Channel 2 at 80.00 MHz. This difference in the configuration resulted in an expected optical beatnote at 1 kHz between the two end-user outputs. The combined optical signal from the fiber coupler was detected on a photodiode (PD), and the DC output of the PD was connected to an oscilloscope to visualize this beatnote. This setup, illustrated in Fig. 14, allowed us to directly measure the residual frequency difference between the two stabilized optical paths. To analyze the spectral properties of this beatnote with higher resolution, I used an acquisition card (ACQ). Unlike a standard spectrum analyzer—which is inherently limited by its resolution bandwidth—the ACQ allows for high sampling rates and a large number of acquisition points. This makes it particularly well-suited for detecting low-frequency signals with narrow spectral

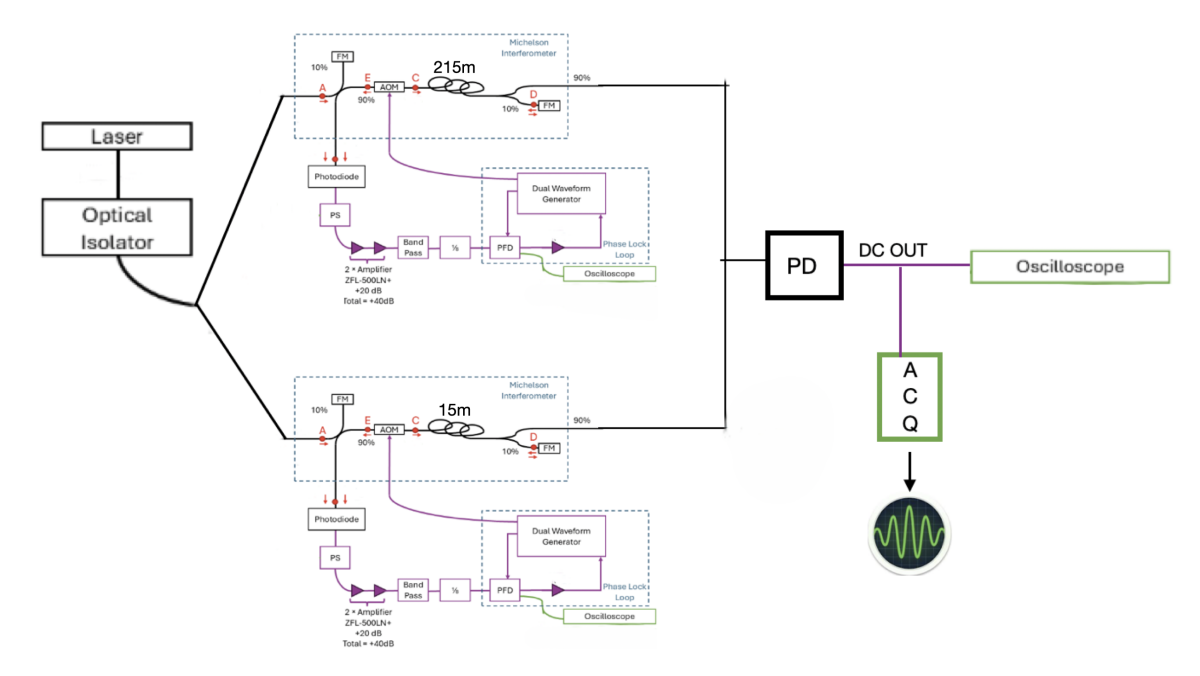


Figure 14: The end-user outputs from the newly implemented and original channels are combined at a photodiode to generate the beat note between them.

linewidths.

To demonstrate this limitation of the spectrum analyzer, I performed a control experiment by inputting a single-frequency signal. Ideally, such a signal should produce a Dirac-like delta function in the frequency domain. However, the spectrum analyzer displayed a broadened spectral peak with a finite linewidth, confirming that its internal resolution bandwidth imposes a limit on spectral accuracy. This validated our choice of using the acquisition card for precise frequency-domain analysis of the beatnote signal.

To ensure accurate frequency analysis, I adhered to the Nyquist criterion, which states that the sampling frequency f_{acq} must be at least twice the signal frequency:

$$f_{\rm acg} \geq 2 \times f_{\rm sig}$$
.

Additionally, the sampling frequency is related to the acquisition parameters by

$$f_{\rm acq} = \frac{N}{T} = \frac{1}{\tau_{\rm acq}},$$

where N is the total number of acquired points, T is the total acquisition time, and τ_{acq} is the time interval between two consecutive samples.

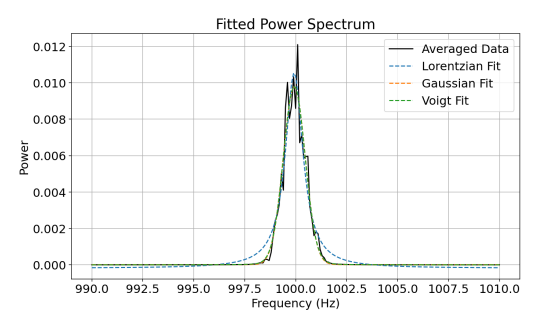
The frequency resolution of the resulting spectrum is given by

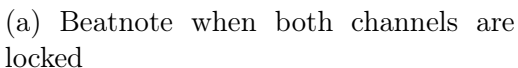
$$\Delta f = \frac{1}{T}.$$

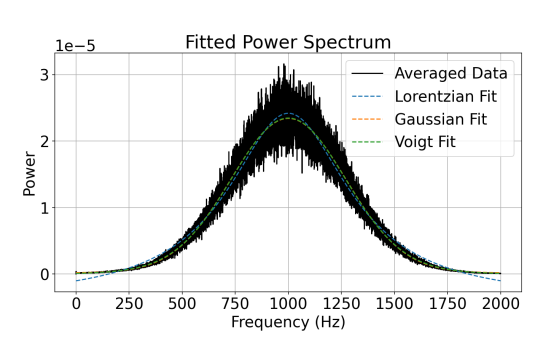
For our measurements, I set T=10 s, yielding a resolution of $\Delta f=0.1$ Hz, which is enough for characterizing sub-Hz-level spectral features. The acquired time-domain data were Fourier transformed to obtain the power spectrum of the beatnote. The

resulting spectrum, shown in Fig. 15a, was fitted using Gaussian, Lorentzian, and Voigt profiles in order to analyze the linewidth of the beatnote between the two phase-stabilized channels. To ensure statistical robustness and minimize noise fluctuations, I performed 100 independent measurements under identical conditions. Each measurement produced a beatnote spectrum, and the final spectrum presented here is the result of averaging all 100 individual spectra. This averaging significantly improved the signal-to-noise ratio and allowed for more reliable profile fitting and linewidth estimation. From the plot shown in Fig. 15a, it is evident that the Voigt profile provides the best fit to the averaged beatnote spectrum. The Gaussian profile also fits reasonably well, but the Lorentzian profile shows significant deviation at the wings of the distribution. According to the fitting parameters returned by the code—and as visually confirmed on the plot—the full width at half maximum (FWHM) is approximately 0.55 Hz for the Voigt fit and 0.59 Hz for the Gaussian fit. This indicates that the beatnote between the two phase-stabilized channels has a linewidth well below 1 Hz, demonstrating excellent performance of the phase noise compensation system.

For comparison, a second measurement was carried out under identical conditions, but with the long arm (215 m) left uncompensated (i.e., the phase lock loop was disabled). The resulting spectrum is shown in Fig. 15b. Even after averaging 100 spectra, the beatnote exhibits significantly broader linewidth and higher noise levels. The FWHM extracted from the Voigt fit in this case is approximately 270 Hz. This confirms that without phase noise compensation, fluctuations in the optical path length introduce substantial broadening, and highlights the effectiveness of the implemented stabilization scheme.







(b) Beatnote when long Channel (215m is unlocked)

Figure 15

7.4 Graphical user interface for the Optical Signal Stabilization system

The experimental setup consisted of three independent phase noise compensation channels, each dedicated to a different team and equipped with its own set of instruments. To improve usability and efficiency, we aimed to make the entire system remotely controllable via a centralized web-based graphical user interface (GUI).

The interface was designed to allow users to configure synthesizers, monitor realtime plots from the oscilloscope, and verify the locking status of the system.

One of the most time-consuming yet critical tasks I undertook was the development of the control software. This involved writing communication protocols for each instrument, configuring them based on experimental needs, and extracting real-time data from the oscilloscope to visualize the error signal. I initially adapted a GUI framework developed by Pierre Cladé, which served as a starting point, and significantly extended it to integrate my custom control scripts and instrument synchronization.

After considerable effort, I successfully implemented a fully operational remote interface, shown in Fig. 16. The GUI provides interactive control over several key parameters:

- **AOM Frequency:** This is the initial frequency applied to the acousto-optic modulator (AOM). Once set, it automatically determines the reference frequency as AOM freq/4.
- **PLL Gain:** This represents the gain of the phase-locked loop applied to the synthesizer. The synthesizer frequency is updated as:

$$f_{\text{synth}}(t) = f_c + G_{\text{PLL}} \cdot \varphi_{\text{error}}(t),$$

where f_c is the AOM frequency and $\varphi_{\text{error}}(t)$ is the error signal obtained from the phase-frequency detector (PFD).

- Level: This sets the driving voltage of the AOM. Prior experimental calibration showed that optimal diffraction occurs at approximately 90 mV $_{\rm RMS}$.
- Freq Shift: A small artificial offset added to the AOM frequency, used as a test to validate the correct functioning of the PFD. When activated via the *Test* button, the system introduces this shift, and triangular waveforms are expected on the display, confirming proper PLL behavior.
- Lock/Unlock: A toggle control that enables or disables the PLL. When locked, the loop actively compensates for phase fluctuations; when unlocked, the compensation is turned off.

The display also includes a **Beatnote Level (mV_{RMS})**, which is currently generated randomly with a timestamp to verify real-time updates. In the final implementation, this will be replaced by a measurement from the actual beatnote detection instrument.

Thanks to this implementation, each team can now securely access the compensation system through a dedicated web interface using a username and password. From their office, lab, or even remotely from home via a phone or computer, users can configure parameters, test system behavior, and monitor locking status in real time—making collaborative operation highly flexible and efficient.

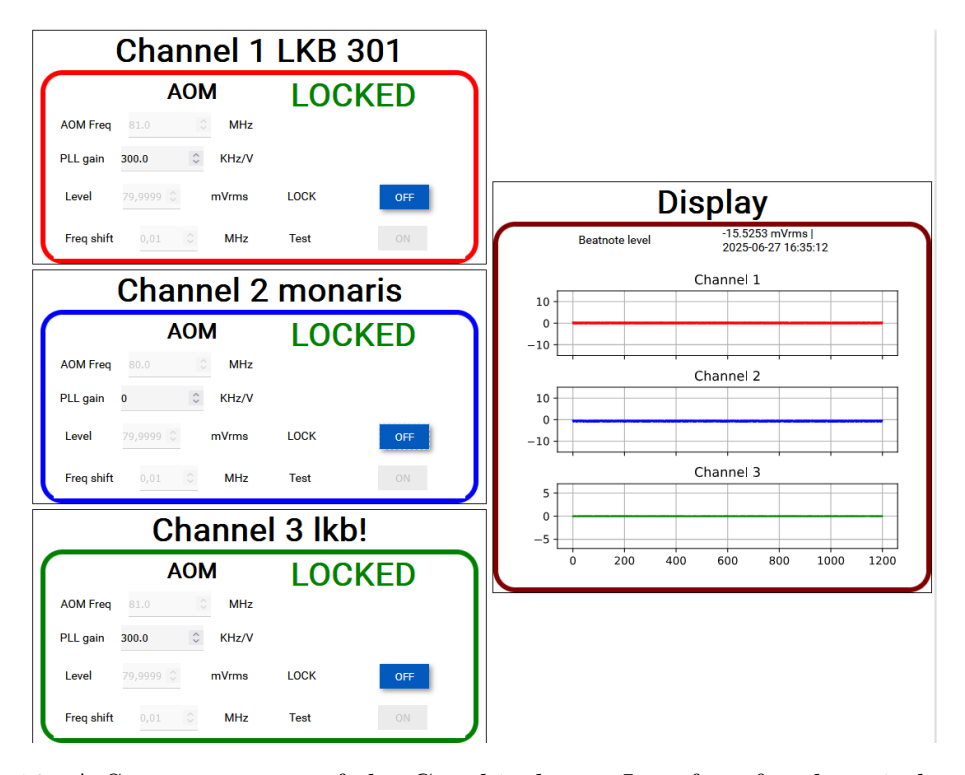


Figure 16: A Screen capture of the Graphical user Interface for three independent phase compensation channels.

8 Future Work and General Remarks

8.1 Future Perspectives

Following the discussions with astrophysicists, the next critical step is to select a scheme that targets a transition highly sensitive to variations in the proton-to-electron mass ratio μ . This choice will determine the exact wavelength region in which we must operate, allowing us to proceed with the acquisition of the appropriate mid-infrared (MIR) laser sources.

Once the MIR laser is obtained, the subsequent phase will involve setting up the required optical cavities, aligning the lasers, and implementing the complete experimental configuration necessary for high-precision NH₃ spectroscopy. All of this will constitute the core of the Ph.D. project that I will be pursuing in the same research team.

General Remarks on the Work

This internship began with a deep dive into the physics of the ammonia molecule and its spectral properties. A significant part of the work involved an extensive bibliographic study to understand the notations, transition types, and experimental methods historically used to probe fundamental constants via molecular spectroscopy.

I also became familiar with various spectroscopic databases, analyzing their structure, notation conventions, and data acquisition methodologies to extract mean-

ingful information for our study.

In the framework of this collaborative project, we held approximately four joint meetings with our partners at Laboratoire de Physique des Lasers (LPL) and the MONARIS laboratory. In each meeting, I presented the latest results of my investigation, which served as the basis for our team discussions and strategic decisions.

I would like to express my sincere gratitude to my supervisor, **Laurent Hilico**, for his continuous support, guidance, and insightful advice throughout this internship. I also thank **Bérengère Argence**, an engineer in our team, with whom I collaborated on the optical signal stabilization aspect of the project.

I am excited to continue this research journey as part of my upcoming Ph.D. thesis within the same team.

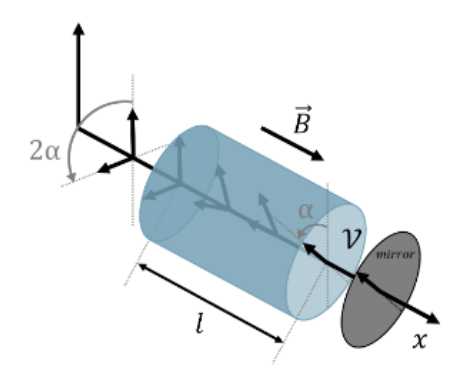


Figure 17: A schematic Faraday mirror. The angle between the incident and the transmitted polarization is 2α . [25]

Appendix

Faraday Mirror

A Faraday mirror is the combination of a Faraday rotator and a standard mirror. As its name suggests, the mirror simply reflects the incoming optical signal, while the Faraday rotator exploits the Faraday effect to manipulate the polarization state of the light.

The Faraday effect causes an optically inactive medium—typically a material like terbium gallium garnet (TGG)—to become birefringent in the presence of a static magnetic field \vec{B} . This results in a rotation of the polarization of linearly polarized light as it propagates through the medium. The rotation angle α is proportional to the magnetic field strength B, the propagation length l, and a material-specific constant known as the Verdet constant V. This relationship is given by:

$$\alpha = V \cdot l \cdot B \tag{3}$$

The Faraday mirrors used in this setup are designed to induce a 45° rotation of the polarization of the incoming signal during both the forward and return paths. As a result, the reflected polarization becomes orthogonal to the input polarization. This feature ensures that the returning beams from both arms of the interferometer arrive at the photodetector with matching polarization states, thereby optimizing interference contrast and ensuring stable detection.

Acousto-Optic Modulator (AOM)

An acousto-optic modulator (AOM) enables shifting the frequency and phase of an optical signal using sound waves.

Via the piezoelectric effect, an electric signal drives a ceramic transducer to vibrate. This vibration generates sound waves in a quartz crystal, inducing periodic modulation of the refractive index given by:

$$n(x,t) = n_0 + n_1 \cos(\Omega t - k_{AOM} x)$$

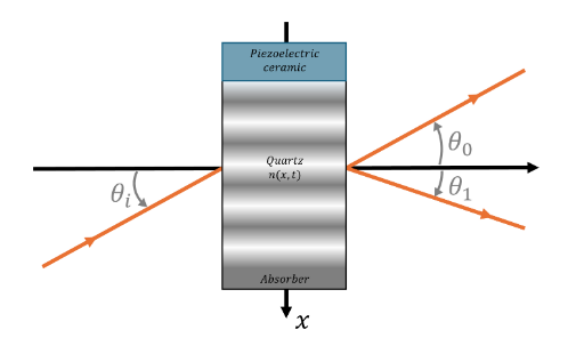


Figure 18: A schematic AOM. The incident angle is θ_i . The diffraction order 1 angle is θ_1 .[25]

where $\Omega = 2\pi f_{AOM}$, $k_{AOM} = \frac{2\pi f_{AOM}}{v}$, v is the speed of sound in quartz, and x the sound wave propagation direction.

These sound waves form a dynamic diffraction grating. Conservation of energy and momentum leads to the diffraction angles θ_p (for each order $p \in \mathbb{Z}$), satisfying:

$$\sin \theta_p = \sin \theta_i + p \cdot \frac{\lambda_i}{\lambda_{\text{AOM}}}$$
 and $\cos \theta_p = \cos \theta_i$

where λ_i is the wavelength of the optical signal and λ_{AOM} is the acoustic wavelength. When the incident beam hits the AOM at Bragg's angle, the diffraction simplifies to:

$$\sin \theta_p = p \cdot \frac{\lambda_i}{2\lambda_{\text{AOM}}}$$

In our setup, we use a fiber-coupled AOM operating at $f_{AOM} = 80$ MHz, where the first-order diffracted beam is coupled into the output fiber. This results in:

$$\omega_p = \omega_i + \Omega$$
 and $f_p = f_i + f_{AOM}$

where ω_p and f_p are the angular frequency and frequency of the diffracted beam, respectively, and ω_i , f_i those of the incident beam.

The optimal driving amplitude for the AOM was experimentally found to be around 90 mV_{pp} (peak-to-peak) by plotting output power versus voltage [25]. The AOM has a frequency acceptance bandwidth of approximately ± 2 MHz at half maximum.

Photodiode and Beatnote

A photodiode is a semiconductor diode that produces an electrical signal when it absorbs photons. It can be used to detect the beatnote produced by two interfering optical fields \vec{E}_1 and \vec{E}_2 , defined as:

$$\mathbf{E}_1 = E_0^{(1)} \, \boldsymbol{\varepsilon}_1 \, e^{i(\omega_1 t - \mathbf{k}_1 \cdot \mathbf{r} + \phi_1)} \qquad \text{and} \qquad \mathbf{E}_2 = E_0^{(2)} \, \boldsymbol{\varepsilon}_2 \, e^{i(\omega_2 t - \mathbf{k}_2 \cdot \mathbf{r} + \phi_2)}$$

where ω_1 , ω_2 are the angular frequencies, \mathbf{k}_1 , \mathbf{k}_2 are the wave vectors, ϕ_1 , ϕ_2 are the phases, and $\boldsymbol{\varepsilon}_1$, $\boldsymbol{\varepsilon}_2$ are the polarization vectors of the two fields.

When both fields are guided into the same optical fiber and reach the photodiode, the total electric field is the sum:

$$\mathbf{E}_3 = \mathbf{E}_1 + \mathbf{E}_2$$

The photodiode measures the intensity of this total field, given by:

$$I = |\mathbf{E}_3|^2 = (\mathbf{E}_1 + \mathbf{E}_2)(\mathbf{E}_1^* + \mathbf{E}_2^*)$$

$$= |\mathbf{E}_1|^2 + |\mathbf{E}_2|^2 + 2\operatorname{Re}\left[E_0^{(1)}(E_0^{(2)})^* \boldsymbol{\varepsilon}_1 \cdot \boldsymbol{\varepsilon}_2^* e^{i[(\omega_1 - \omega_2)t - (\mathbf{k}_1 - \mathbf{k}_2) \cdot \mathbf{r} + (\phi_1 - \phi_2)]}\right]$$

The beat signal detected by the photodiode is the oscillating term at the frequency difference $\omega_1 - \omega_2$, and is given by:

$$s_{\text{beat}}(\mathbf{r}, t) = U \cdot \cos\left[(\omega_1 - \omega_2)t - (\mathbf{k}_1 - \mathbf{k}_2) \cdot \mathbf{r} + (\phi_1 - \phi_2)\right]$$

where U is an amplitude factor proportional to the product of the electric field amplitudes and polarization overlap.

References

- [1] P. A. M. Dirac. In: Nature (London) 139 (1937), p. 323.
- [2] J. K. Webb et al. "Further Evidence for Cosmological Evolution of the Fine-Structure Constant". In: *Phys. Rev. Lett.* 87.9 (2001), p. 091301.
- [3] E. Reinhold et al. "Stringent Test of a Time Variation of the Fine-Structure Constant Using Many H2 Lines". In: *Phys. Rev. Lett.* 96.15 (2006), p. 151101.
- [4] W. Ubachs et al. "Laboratory and astrophysical probes of a possible variation of the proton-to-electron mass ratio". In: Rev. Mod. Phys. 88.2 (2016), p. 021003. DOI: 10.1103/RevModPhys.88.021003. arXiv: 1511.04476 [astro-ph.GA].
- [5] P. Jansen, H. L. Bethlem, and W. Ubachs. "Perspective: Tests of fundamental constant variation with molecules". In: J. Chem. Phys. 140 (2014), p. 010901.
- [6] V. Špirko. "On the possible variation of the electron-to-proton mass ratio from observations of methanol in the early Universe". In: *J. Phys. Chem. Lett.* 5 (2014), pp. 919–923.
- [7] A. Owens et al. "Ab initio rovibrational spectroscopy of CH3OH and 13CH3OH".
 In: Mon. Not. R. Astron. Soc. 450 (2015), pp. 3191–3206.
- [8] Philip R. Bunker. *Molecular Symmetry and Spectroscopy*. United Kingdom edition. 24/28 Oval Road, London NW1 7DX, United Kingdom: Academic Press Inc. (London) Ltd, 1979.
- [9] Michael J. Down et al. "Re-analysis of ammonia spectra: Updating the HI-TRAN ¹⁴NH₃ database". In: Journal of Quantitative Spectroscopy and Radiative Transfer 130 (2013). Departments: a) University College London, UK; b) Jet Propulsion Laboratory, USA; c) LISA, France, pp. 260–272. DOI: 10.1016/j.jqsrt.2013.06.014.
- [10] S. A. Levshakov et al. "Probing the electron-to-proton mass ratio gradient in the Milky Way with Class I methanol masers". In: *Mon. Not. Roy. Astron. Soc.* 511 (2022), pp. 413–424.
- [11] M. Daprà et al. "Testing the variability of the proton-to-electron mass ratio from observations of methanol in the dark cloud core L1498". In: *Mon. Not. R. Astron. Soc.* 472 (2017), pp. 4434–4443.
- [12] S. Muller et al. "A study of submillimeter methanol absorption toward PKS 1830-211: Excitation, invariance of the proton-electron mass ratio, and systematics". In: A & A 652 (2021), A5.
- [13] R. Lange et al. "Improved Limits for Violations of Local Position Invariance from Atomic Clock Comparisons". In: *Phys. Rev. Lett.* 126 (2021), p. 011102.
- [14] A. Shelkovnikov et al. "Stability of the proton-to-electron mass ratio". In: *Phys. Rev. Lett.* 100 (2008), p. 150801.
- [15] J. Kobayashi et al. "Measurement of the variation of electron-to-proton mass ratio using ultracold molecules produced from laser-cooled atoms". In: *Nat. Commun.* 10 (2019), p. 3771.

- [16] V. V. Flambaum and M. G. Kozlov. "Limit on the Cosmological Variation of m_p/m_e from the Inversion Spectrum of Ammonia". In: *Physical Review Letters* 98.24 (2007), p. 240801.
- [17] J. Vorotyntseva et al. "Methanol isotopologues as a probe for spatial and temporal variations of the electron-to-proton mass ratio". In: *Mon. Not. Roy. Astron. Soc.* 527 (2024), pp. 2750–2755.
- [18] P. Jansen et al. "Methanol as a sensitive probe for spatial and temporal variations of the proton-to-electron mass ratio". In: Phys. Rev. Lett. 106 (2011), p. 090801.
- [19] A. Owens et al. "Enhanced sensitivity to a possible variation of the proton-toelectron mass ratio in ammonia". In: *Phys. Rev. A* 93 (2016), p. 052506.
- [20] Maria N. Drozdovskaya et al. "Low NH3/H2O ratio in comet C/2020 F3 (NE-OWISE) at 0.7 au from the Sun". In: Astronomy & Astrophysics 677 (2023), A157.
- [21] S. Urban et al. "Pure rotational spectrum of the ν_2 vibrational state of ammonia". In: J. Mol. Spectrosc. 79 (1980), pp. 455–480.
- [22] H. Sasada et al. "Carbon dioxide laser spectroscopy of the ν_2 band of ammonia". In: *J. Mol. Spectrosc.* 96 (1982), pp. 106–115.
- [23] H. Sasada et al. "Pure rotational transitions of the ν_4 vibrational state of ¹⁴NH₃". In: *J. Mol. Spectrosc.* 151 (1992), pp. 33–45.
- [24] Long-Sheng Ma et al. "Delivering the same optical frequency at two places: accurate cancellation of phase noise introduced by an optical fiber or other time-varying path". In: *Optics Letters* 19.21 (1994), pp. 1777–1779. DOI: 10. 1364/OL.19.001777. URL: https://doi.org/10.1364/OL.19.001777.
- [25] Y. Baron and M. Comba. Phase Noise Compensation in Optical Fiber. Mines Paris – PSL — Research Trimester — School year 2024–2025. 2025.